Acta Materialia 183 (2020) 340–349

Contents lists available at ScienceDirect

Acta Materialia

journal homepage: www.elsevier.com/locate/actamat

Full length article

Growth evolution and formation mechanism of η'-Cu_6Sn_5 whiskers on η-Cu_6Sn_5 intermetallics during room-temperature ageing

Z.H. Zhang[a,b,*], C.W. Wei[a,b], J.J. Han[b,a], H.J. Cao[c], H.T. Chen[d], M.Y. Li[d]

[a] Fujian Key Laboratory of Advanced Materials, College of Materials, Xiamen University, Xiamen, 361005, China
[b] Shenzhen Research Institute of Xiamen University, Shenzhen 518055, China
[c] School of Mechanical and Automation Engineering, Xiamen City University, Xiamen 361005, China
[d] College of Material, Harbin Institute of Technology (Shenzhen), Shenzhen 518055, China

ARTICLE INFO

Article history:
Received 6 August 2019
Revised 8 November 2019
Accepted 11 November 2019
Available online 14 November 2019

Keywords:
Whiskers
Phase transformation
Intermetallic compounds
Ab initio molecular dynamics
Transmission electron microscopy

ABSTRACT

The phase-transformation-induced damage of Cu_6Sn_5 is an emerging reliability issue in the manufacturing of 3D ICs. Although the retarded phase transformation from η-Cu_6Sn_5 to η'-Cu_6Sn_5 at room temperature can produce a large expansion in volume, how the transformation stress threatens the joint reliability during usage is poorly understood. In this paper, the evolution characteristics of quenched η-Cu_6Sn_5 bumps were observed during ageing at 25 °C for 1–40 d Due to the retarded phase transformation, η'-Cu_6Sn_5 whiskers spontaneously nucleated and grew on the surfaces of η-Cu_6Sn_5 bumps. The orientation relationship between the two phases favourable for whisker growth was confirmed, and two necessary conditions for whisker formation were discussed. In addition, the potential harmfulness of whisker growth was analysed. The study will help expose the phase-transformation-induced damage of Cu_6Sn_5 during room-temperature ageing and may reduce the failure risk of entire Cu_6Sn_5 intermetallic joints in future large-scale applications of 3D ICs.

1. Introduction

Three-dimensional integrated circuits (3D ICs), which merge chip technology and packaging technology, are considered to have potential applications in overcoming the scaling limits in super-large-scale integration (SLSI) [1,2]. The two most typical features of this technology are (1) continuous minimization of the interconnection size on a limited chip area and (2) vertical stacking of multi-chips in a tight device space. The first feature causes downsizing of Sn-based solder bumps (Sn bumps); some scholars further predict that if a Sn bump can be reduced in size from the current 100 μm to 1 μm in the future, then the interconnection density per unit area would sharply rise by 4 orders of magnitude [3,4]. However, following this downsizing tendency, a large volume fraction of Cu_6Sn_5 intermetallics (IMCs) will also form at the Sn-bump|Cu-through-Si-via (Sn-bump|Cu-TSV) interfaces during reflow [5–9]. Because the average diameter of Cu_6Sn_5 grains is 1–2 μm after the traditional reflow process, a resultant Sn-bump|Cu-TSV joint may currently contain only a few Cu_6Sn_5 grains and even a single grain in the future [10]. Such joints will be increasingly dependent on Cu_6Sn_5 IMCs and will be highly anisotropic [11,12]. Interestingly, if a Sn-bump|Cu-TSV joint is entirely composed of Cu_6Sn_5, a joint with a melting point up to 415 °C can be achieved [7,13]. During the chip stacking process, an interconnection with high-melting-point joints can avoid the re-melting and collapse of Sn bumps at lower levels, bear the weight of additional chips, and maintain the standoff height between adjacent chips for heat dissipation [14]. In brief, entire Cu_6Sn_5 IMC joints can provide strong mechanical support for fabrication of vertically stacked structures, satisfying the second feature of 3D ICs.

The formation of entire Cu_6Sn_5 IMC joints for multi-chip interconnections seems to be an irresistible trend in 3D ICs. However, some scholars [15–19] are worried that although this improvement can achieve satisfactory mechanical (*e.g.*, compressive and bonding) strengths, the brittleness of Cu_6Sn_5 may trigger crack initiation and propagation, posing a serious threat to joint reliability. Essentially, the crack damage of Cu_6Sn_5 is induced by interfacial stresses, such as peeling stress under shock or vibration [20–23], electric stress under current stressing [24–27], and thermal-

* Corresponding author at: Fujian Key Laboratory of Advanced Materials, College of Materials, Xiamen University, Xiamen, 361005, China.
E-mail addresses: Zhzhang@xmu.edu.cn (Z.H. Zhang), Jiajiahan@xmu.edu.cn (J.J. Han), Chenht@hit.edu.cn (H.T. Chen).

https://doi.org/10.1016/j.actamat.2019.11.032
1359-6454/

mechanical stress under thermal shock or cycling [23,28,29]. Most of the stress-induced damage can be restricted or prevented by using appropriate methods (*e.g.*, under-bump-metallization technology can restrain peeling stresses [27,30], while underfill technology can suppress thermal and mechanical stresses [31]), and these methods may become increasingly effective with the downsizing of interconnection joints. However, Nogita et al. reported a novel damage mode originating from the solid-state phase transformation of Cu_6Sn_5 [2,7,32–34], which seems difficult to avoid. Cu_6Sn_5 exists in at least 2 crystal structures in the solid state [2,35]. The η-Cu_6Sn_5 phase with a space group of $P6_3/mmc$ is expected to transform to the η'-Cu_6Sn_5 phase with a space group of C2/*c* below 186–189 °C. However, this transformation has always been kinetically hindered due to the insufficient reaction time during cooling [36]; the retarded transformation may result in a large expansion in volume, producing severe internal stresses that threaten the joint reliability during usage [32]. Because smaller joints have higher cooling rates, the onset probability of this retarded transformation may rise with decreasing joint size; for example, when the joint size is smaller than 337.5 μm, the metastable η-Cu_6Sn_5 phase may be completely maintained at room temperature after a traditional reflow process (*see the Supporting Information*). Accordingly, the phase-transformation-induced damage of Cu_6Sn_5 may become one of the most critical failure modes in future large-scale applications of 3D ICs.

Despite the danger of this unusual damage mode, the experimental observation of Cu_6Sn_5 growth evolution during phase transformation from η-Cu_6Sn_5 to η'-Cu_6Sn_5 has seldom been reported, and an in-depth understanding of the formation mechanism (*e.g.*, kinetics and crystallography) and the corresponding influence on crack initiation and propagation is still lacking. This paper has the following three objectives: to determine the characteristic of whisker growth during Cu_6Sn_5 phase transformation, to discuss the formation mechanism and to analyse the phase-transformation-induced damage and potential inhibition methods.

2. Experimental procedure

2.1. Sample preparation

For ease of observation of the microstructural evolution, Cu_6Sn_5 IMC bumps, rather than Cu_6Sn_5 flip-chip joints, were fabricated by the soldering reaction between polycrystalline Cu sheets and Sn-0.7wt%Cu liquid solder at 250 °C. Because the accumulation of compressive stress inside Cu_6Sn_5 bumps will be directly related to the volume of the metastable η-Cu_6Sn_5 phase, the small Cu_6Sn_5 bumps may not exhibit a sufficient compressive stress to promote the η'-Cu_6Sn_5 whisker growth; accordingly, a long-lasting soldering reaction is needed to obtain large Cu_6Sn_5 bumps. After 10 h of soldering reaction, the liquid solder on the Cu sheets was blown away by compressed N_2 gas (120 psi). The resultant sheets were quenched to 0 °C, and the residual solder was selectively removed by a 10% chemical etching solution of nitric acid in ethyl alcohol. The as-prepared sheets were then rinsed in distilled ice water in an ultrasonic bath for 1 min, dried under N_2 gas, and aged at 25 °C for 1–40 d

2.2. Sample characteristics

At each selected time point (*i.e.*, 1, 20 and 40 d), the microstructures of the as-prepared sheets were characterized by scanning electron microscopy (SEM, Hitachi S-4800), X-ray diffractometry (XRD, Rigaku D/max-2500 PC) and Auger electron spectroscopy (AES, Ulvac-Phi PHI-700). Note that the X-ray source came from Cu $K\alpha$ radiation (λ = 1.5406 Å) at a high voltage of 40 kV and a current of 100 mA, and the XRD data were collected in the 2θ range of 25–80° with a scan rate of 0.5°/min at room temperature. Moreover, differential scanning calorimetry (DSC, Netzsch STA-449F3) tests were conducted with two consecutive heating-cooling cycles in the temperature range of 25–220 °C at a rate of 1 °C•min^{-1} in air. All the DSC samples were peeled from the shallow surfaces of the as-prepared sheets after thermal ageing, and the weight of each sample was 30 mg. In addition, to study the growth characteristics and transformation mechanism of η'-Cu_6Sn_5 on η-Cu_6Sn_5 IMCs, the as-prepared sheet after thermal ageing for 40 d was cut using a focused-ion beam (FIB, FEI Helios NanoLab 600i), and the surface microstructures were observed by high-resolution transmission electron microscopy (HR-TEM, Philips Tecnai G2 F20).

2.3. Simulation method

To explore the transformation mechanisms of the kinetics and crystallography, *ab initio* molecular dynamics (AIMD) simulations were conducted on the basis of density functional theory and implemented using the Vienna *ab initio* simulation package (VASP). The Perdew-Burke-Ernzerhof exchange-correlation functional was employed with projector augmented wave pseudopotentials [37,38]. The simulations were performed in a canonical ensemble with velocity scaling for temperature control, and the pressure-volume curve was adopted to ensure that the average pressure was equal to the expected value (*i.e.,* 0 here) for the simulation under constant pressure. The equation of motion was solved via the velocity Verlet algorithm with a time step of 1 fs. Two rectangular supercells with 416 and 412 atoms for the $(1\bar{2}10)_{\eta}|(102)_{\eta'}$ and $(1\bar{2}10)_{\eta}|(3\bar{5}6)_{\eta'}$ interfaces, respectively, were constructed as the initial configuration and heated to 400 K. Both simulations were performed for 2000 steps, and the von Mises strain was adopted as a measure of the plastic deformation at the atomic level.

3. Results

3.1. Surface microstructural evolution of Cu_6Sn_5 IMC bumps

Fig. 1 shows the evolution of the surface microstructure of the as-prepared sheet after ageing at 25 °C for 1–40 d After ageing for 1 d (Fig. 1a), a layer of hill-like bumps with smooth surfaces is observed on the original polycrystalline Cu sheet. The AES analysis confirms that these hill-like bumps have a stoichiometric composition of $Cu_{6.4}Sn_5$, implying that Cu_6Sn_5 IMCs have been generated on the Cu sheet after the soldering reaction. Moreover, based on the inverse pole figure (IPF) map obtained by electron backscatter diffraction (EBSD), each bump is identified as a single crystal. In addition, the average diameter of these single-crystal bumps ranges from 20 to 30 μm, as shown in the insert in Fig. 1a.

After ageing for 20 d (Fig. 1b), the surfaces of the hill-like bumps are no longer smooth, and numerous protuberance-like structures with diameters of 0.2–0.3 μm and some microcracks spontaneously emerge in certain areas of the bump surfaces. Furthermore, after ageing for 40 d (Fig. 1c), the original Cu_6Sn_5 bumps cannot be identified on the Cu sheet, and the entire sheet is supplanted by clusters of whisker-like structures with lengths of 5–10 μm and diameters of 0.3–0.5 μm. Note that the newly generated structures have stoichiometric compositions of $Cu_{6.1}Sn_5$ and $Cu_{5.9}Sn_5$ for 20 and 40 d of ageing, respectively; no O element is detected, indicating that these structures are not Cu_6Sn_5 oxides but are instead evolution products. In addition, considering that very large changes in the surface microstructures and a slight change in the chemical composition between the original Cu_6Sn_5 bumps and newly generated structures are found, we believe that the Cu_6Sn_5 bumps on the as-prepared sheet have spontaneously undergone a reconstruction of the surface microstructures with little change in the chemical composition during room-temperature ageing.

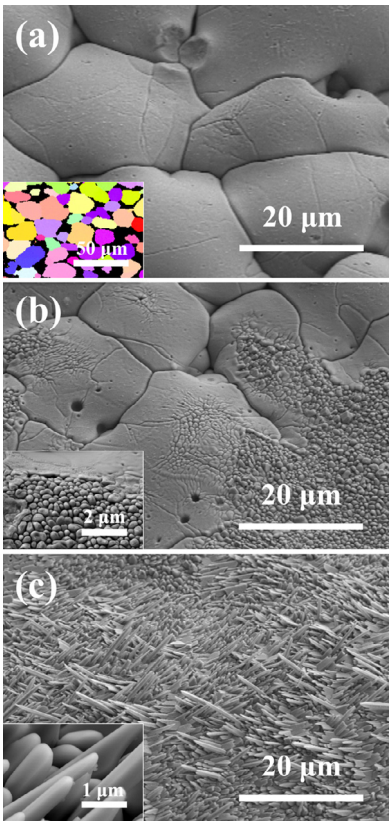

Fig. 1. Typical micrographs of the surface microstructural evolution on the same as-prepared sheet after ageing at 25 °C for (a) 1 d, (b) 20 d, and (c) 40 d The inserted IPF map in (a) shows the top-down view of another as-soldered sheet after polishing. A hexagonal structure of the η-Cu_6Sn_5 phase (space group of $P6_3/mmc$, $a = b = 4.192$ Å, $c = 5.037$ Å, and $\gamma = 120°$) was used in this EBSD analysis. In addition, the inserted SEM images in (b) and (c) are enlarged fragmentary views of (b) and (c), respectively.

3.2. Surface orientation evolution of Cu_6Sn_5 IMC bumps

Fig. 2 shows XRD patterns of the surface layers on the same as-prepared sheet after ageing at 25 °C for 1–40 d. The Rietveld refinement was carried out using EXPGUI–GSAS software (*see the Supporting Information*). Based on the International Centre for Diffraction Data (ICDD) card No. 00–004–0836, the three main diffraction peaks at 43.29° $(111)_{Cu}$, 50.43° $(100)_{Cu}$ and 74.12° $(110)_{Cu}$ in *line a* can be indexed to the Cu phase (*Fm*-3 m), indicating that the Cu sheet is indeed polycrystalline. However, after soldering for 10 h and then ageing at 25 °C for 1–40 d, the original diffraction peaks of the Cu phase dramatically diminish, and many new diffraction peaks are observed in *lines b-d*. Due to the fast growth of the interfacial IMCs during soldering, the original Cu peaks eventually disappear when the Cu_6Sn_5 layer grows sufficiently thick; thus, the generated diffraction peaks in *lines b-d* are likely attributed to the formation of Cu_6Sn_5. By careful comparison of ICDD cards and our XRD patterns, the diffraction peaks of the as-prepared sheet after ageing for 1 d (*line b*) basically match those of the η-Cu_6Sn_5 phase ($P6_3/mmc$, ICDD card No. 01–071–5036). The diffraction peaks of the as-prepared sheet after ageing for 40 d (*line d*) closely match those of the η'-Cu_6Sn_5 phase ($C2/c$, ICDD card No. 01–072–8761), and the diffraction peaks of the as-prepared sheet after ageing for 20 d (*line c*) are mixtures of those of both the metastable η-Cu_6Sn_5 and stable η'-Cu_6Sn_5 phases. Therefore, the Cu_6Sn_5 bumps on the as-prepared sheet should undergo a phase transformation from η-Cu_6Sn_5 to η'-Cu_6Sn_5 during room-temperature ageing.

Moreover, in the 2θ range of 29.5–30.5°, the strong diffraction peak at 30.271° in *line b* is assigned to $(101)_\eta$, slightly deviating from its standard position (30.323°) in the η-Cu_6Sn_5 phase. The extremely weak diffraction peak at 30.153° in *line d* is assigned to $(\bar{1}13)_{\eta'}$, perfectly matching its standard position (30.157°) in the η'-Cu_6Sn_5 phase. The moderately strong diffraction peak at 30.220° in *line c* is relatively broad and asymmetric and should be induced by a superposition of the two diffraction peaks centred at 30.157° (the standard $(\bar{1}13)_{\eta'}$ peak) and 30.220° (the distorted $(101)_\eta$ peak). Similarly, in the 2θ range of 42–44°, the strong diffraction peak at 43.652° in *line b* is assigned to $(102)_\eta$, slightly deviating from its standard position of 43.708°. The strong diffraction peak at 42.962° in *line d* is assigned to $(204)_{\eta'}$, closely matching its standard position of 43.000° The broad peak at 43.385° in *line c* can be divided into two peaks centred at 43.321° (the standard $(\bar{3}14)_{\eta'}$ peak) and 43.614° (the distorted $(102)_\eta$ peak). Suh et al. proposed that in a solid-state phase transformation, the product phase preferentially maintains a coherent/semi-coherent relationship with the parent phase to minimize the interfacial energy [39]; therefore, orientation relationships between η-Cu_6Sn_5 and η'-Cu_6Sn_5 can be determined, *e.g.*, $(101)_\eta \| (\bar{1}13)_{\eta'}$, $(102)_\eta \| (\bar{3}14)_{\eta'}$, and $(110)_\eta \| (204)_{\eta'}$ [35]. However, based on the intensity of the diffraction peaks in *lines b-d*, the actual evolution rule of the preferred orientations for this transformation is $(101)_\eta + (102)_\eta \rightarrow (204)_{\eta'}$, rather than $(101)_\eta + (102)_\eta \rightarrow (\bar{1}13)_{\eta'} + (\bar{3}14)_{\eta'}$. Because a dramatic change in the preferred orientation occurs, we believe that the Cu_6Sn_5 bumps undergo a reconstruction of the surface orientation during the phase transformation.

In addition, all the diffraction peaks in *line b* and the diffraction peaks assigned to the η-Cu_6Sn_5 phase in *line c* have slight deviations to lower diffraction angles compared to those of the standard ICDD card of the η-Cu_6Sn_5 phase. However, all diffraction peaks in *line d* and diffraction peaks assigned to the η'-Cu_6Sn_5 phase in *line c* perfectly agree with the standard ICDD card of the η'-Cu_6Sn_5 phase. Based on Castro's work [40], a reduction in the diffraction angle corresponds to a biaxial in-plane compressive stress in the layer, which would increase the out-of-plane interplanar spacing; the larger the compressive stress is, the greater the deviation to a lower diffraction angle. Although the distribution of compressive stresses in the Cu_6Sn_5 bumps may vary with the depth to the surface, grain orientation, and ageing time, our experiments can provide a preliminary, qualitative result suggesting that compressive stresses indeed exist. Interestingly, following Castro's principle, we obtain a surprising inference that compressive stress would accumulate in only the η-Cu_6Sn_5 phase with increasing ageing time and that no additional stress exists inside the η'-Cu_6Sn_5 phase. To satisfy this requirement, the η'-Cu_6Sn_5 phase should not be formed inside the Cu_6Sn_5 bumps but only on the bump surfaces (which can efficiently release the generated transformation stress); thus, we suspect that this phase transformation may be related to the stress condition.

3.3. Phase transformation kinetics of Cu_6Sn_5 IMCs

Fig. 3 shows the DSC heat flow signals of five types of Cu_6Sn_5 samples peeled from the shallow surfaces of as-prepared sheets after ageing for 1–40 d. For *Sample-1d* (Fig. 3a), two endothermic peaks are observed on the first heating curve, but only one remains on the second heating curve. The first cooling curve has two exothermic peaks, and the shape of the second cooling curve perfectly coincides with that of the first one. For *Sample-20d* (Fig. 3b) and *Sample-40d* (Fig. 3c), the curve shapes are basically consistent with those shown in Fig. 3a. However, the following differences are found: (1) The two endothermic peaks on the first heating curve gradually merge into a single peak. (2) The positions of the exothermic peaks in the temperature range of

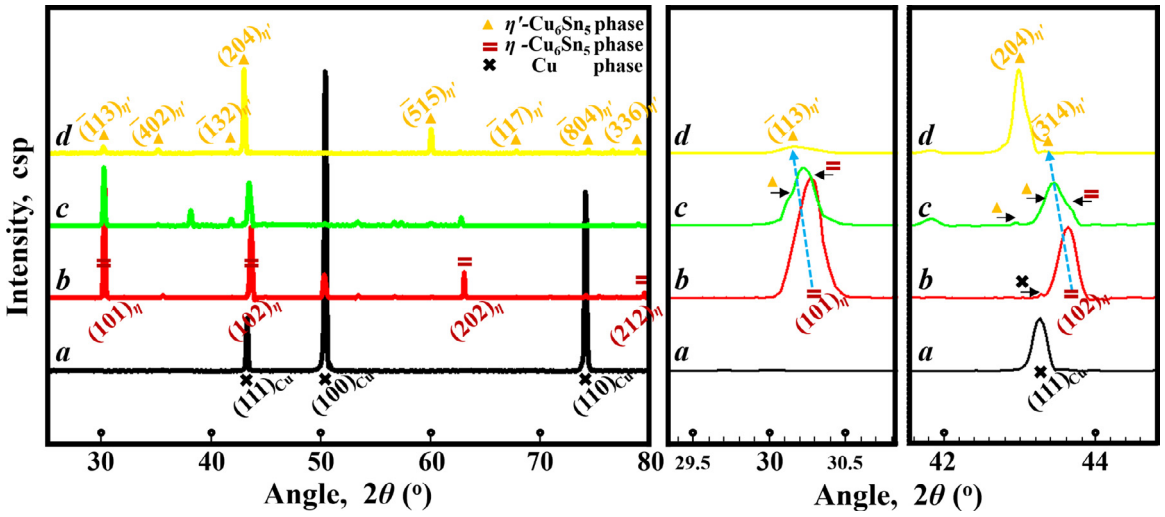

Fig. 2. XRD patterns of the surface layers on the same as-prepared sheet: *a* (black line), the original Cu sheet; *b* (red line), after ageing for 1 d; *c* (green line), after ageing for 20 d; and *d* (yellow line), after ageing for 40 d The diffraction peaks are indexed utilizing the ICDD cards for Cu (00–004–0836), η-Cu_6Sn_5 (01–071–5036), and η'-Cu_6Sn_5 (01–072–8761). In addition, the 2θ ranges of 29.5–30.5° and 42–44° are shown at enlarged scales to magnify the relatively weak diffraction peaks (For interpretation of the references to color in this figure legend, the reader is referred to the web version of this article.).

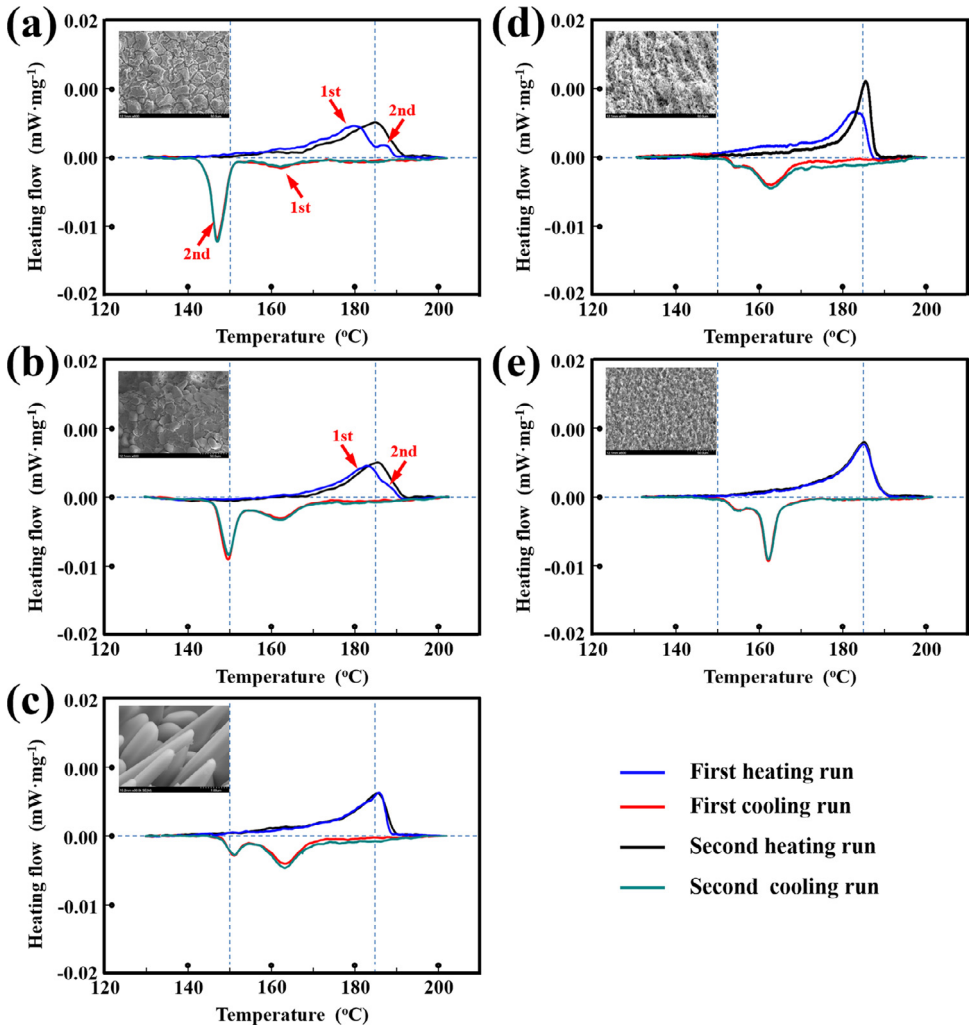

Fig. 3. DSC heating and cooling curves of five Cu_6Sn_5 samples. (a) *Sample-1d*, (b) *Sample-20d*, and (c) *Sample-40d* are peeled from the shallow surfaces of the as-prepared sheets after ageing for 1, 20, and 40 d, respectively. (d) *Sample-1d-p* and (e) *Sample-40d-p* are the ground powder of *Sample-1d* and *Sample-40d*, respectively. The morphologies of particles are provided in the figures, and the powder samples were sifted through a 2800-mesh sieve before use.

160–170 °C change only slightly, but the corresponding areas gradually increase; in contrast, the positions of the exothermic peaks in the temperature range of 145–155 °C slightly shift to higher temperatures, while the corresponding areas sharply decrease. In addition, *Sample-1d-gp* is the ground powder of *Sample-1d*; by comparing the corresponding curves in Fig. 3a and d, visibly dissimilar peak positions and areas before and after the grinding treatment are observed. A similar situation is found in the results of *Sample-40d* (Fig. 3c) and *Sample-40d-gp* (Fig. 3e).

Differences in phase composition and particle size may occur among the initial samples. According to our SEM and XRD results, the Cu_6Sn_5 phase transformation is likely controlled by a nucleation-growth process; the Gibbs free energy change in nucleation is theoretically given by

$$\Delta G = \Delta G_V + \Delta G_I + \Delta G_\varepsilon \quad (1)$$

where ΔG_V, ΔG_I and ΔG_ε are the changes in the volumetric, interfacial and strain energy, respectively, related to nucleation. ΔG_ε is resistant to phase transformation due to steric hindrance; however, when the phase transformation is accompanied by a volumetric change and a residual stress, the situation may be complicated. Based on the virtual work principle (*see the Supporting Information*), when the compressive stress exists, the shrinkage transformation will be promoted due to $\Delta G_\varepsilon<0$, while the dilatational transformation will be retarded due to $\Delta G_\varepsilon>0$.

Because the Cu_6Sn_5 phase transformation is kinetically complete for the temperature change rate of $\leq$1 °C•min^{-1} [34], all the samples in our DSC tests will ideally be entirely composed of the η-Cu_6Sn_5 phase after heating to 220 °C or the η'-Cu_6Sn_5 phase after cooling to 20 °C. Hence, if an initial sample was composed of only the η'-Cu_6Sn_5 phase, then the curves of its two heating-cooling cycles should overlap (as observed in Fig. 3c or e). However, if a certain amount of the η-Cu_6Sn_5 phase exists in an initial sample, then it would transform to the η'-Cu_6Sn_5 phase during heating (>80 °C [35]), producing a compressive stress in particles due to volume expansion. With further heating, the stress in the particle surfaces will be released, while the stress in the particle cores may be maintained. Accordingly, when the shrinkage transformation from η'-Cu_6Sn_5 to η-Cu_6Sn_5 begins (*i.e.*, ΔG=0), $\Delta G_\varepsilon^{Surface}=0$ and $\Delta G_\varepsilon^{Core}<0$; assuming that $\Delta G_I^{Surface}=\Delta G_I^{Core}>0$, we have $\Delta G_V^{Surface}<\Delta G_V^{Core}<0$ and $\Delta T^{Surface}>\Delta T^{Core}>0$. Thus, the η'-Cu_6Sn_5 phase in the particle cores can transform to the η-Cu_6Sn_5 phase at a lower temperature than that in the particle surfaces due to the existence of compressive stress. Therefore, a sample (*e.g., Sample-1d* and *Sample-20d*) with two separate endothermic peaks on the first heating curve should initially contain a certain amount of η-Cu_6Sn_5. Notably, the smaller the amount of η-Cu_6Sn_5 in the initial samples, the less compressive stress can accumulate in the particles; accordingly, the first endothermic peak on the first heating curve for *Sample-20d* is smaller in area and shifted left compared to that for *Sample-1d* In addition, *Sample-1d-gp* has only a broadened endothermic peak (rather than two peaks) on its first heating curve; the reason for this result may be that the powder can easily release compressive stress, triggering the merging of the first peak with the second one.

Moreover, the kinetics of the normal Cu_6Sn_5 phase transformation may also be influenced by the accompanying transformation stress (Fig. 4). For instance, when the dilatational transformation from η-Cu_6Sn_5 to η'-Cu_6Sn_5 occurs during cooling, η'-Cu_6Sn_5 nuclei will cluster on the surfaces of η'-Cu_6Sn_5 particles and then develop towards the cores. The compressive stress will be generated due to the volume expansion. Because the transformation stress can be efficiently released from the surface, we have $\Delta G_\varepsilon^{Surface}=0$; if $\Delta G_I^{Surface}$ is unchanged, both $\Delta G_V^{Surface}$ and $\Delta T^{Surface}$ (belonging to the surface transformation) will be constant. Hence, we can observe that the positions of all first exothermic peaks on the cooling curves in Fig. 3 are stable. However, the compressive transformation stress in particle cores cannot be easily released and may increase with the occurrence of core transformation. Notably, $\Delta G_\varepsilon^{Core}>0$; if $\Delta G_I^{Surface}=\Delta G_I^{Core}$, t $\Delta G_V^{Core}<\Delta G_V^{Surface}<0$ and $\Delta T^{Core}>\Delta T^{Surface}>0$. Therefore, we can observe another exothermic peak (belonging to the core transformation) at a low temperature on the cooling curve. In addition, the smaller the particle size is, the less the stress accumulates in the cores, and the smaller the difference between $\Delta G_V^{Core}$and $\Delta G_V^{Surface}$ or between ΔT^{Core} and $\Delta T^{Surface}$. Hence, we observe a smaller area and a smaller left shift of the second exothermic peak for the powder sample compared to those for the corresponding non-powder sample on the cooling curves (*e.g.*, Fig. 3d and a or Fig. 3e and c). In addition, the second exothermic peak will continuously shift to a lower temperature with increasing cooling rate, even to room temperature; thus, the metastable η-Cu_6Sn_5 phase can be maintained at 25 °C in our experiments. In summary, the kinetics of the Cu_6Sn_5 phase transformation should be both structure dependent and stress dependent.

3.4. Phase transformation crystallography of Cu_6Sn_5 IMCs

Fig. 5a and b show cross-sectional and top-view SEM images, respectively, of a 40-d-aged Cu_6Sn_5 bump after FIB cutting. The thickness of the sample was 68.6 nm, and a TEM experiment was immediately conducted to avoid sample failure. Fig. 5c shows a TEM image of this bump, and a Cu_6Sn_5 whisker can be observed on the bump surface. Similar to Sn whiskers, the Cu_6Sn_5 whisker is a single crystal with a long narrow shank and a pointed tip. Some single-crystal protuberances surrounding this whisker are also detected. In addition, the bump matrix beneath the whisker is not a single crystal, as it originally is in Fig. 1a, and the grain boundaries are observed to spread across the matrix.

The high-magnification TEM images of three regions of interest (marked *A, B* and *C* in Fig. 5c) are shown in Fig. 5d, e and f, respectively. In *region A*, the lattice spacings of 5.095 Å and 3.638 Å correspond to the $(\bar{2}01)_{\eta'}$ and $(0\bar{2}0)_{\eta'}$ planes, respectively. In *region B*, the lattice spacings of 2.1017 Å and 2.548 Å correspond to the $(\bar{1}3\bar{2})_{\eta'}$ and $(40\bar{2})_{\eta'}$ planes, respectively. In *region C*, the lattice spacings of 5.041 Å and 3.630 Å correspond to the $(0001)_\eta$ and $(\bar{1}010)_\eta$ planes, respectively. The abovementioned results are further verified by the corresponding selected area electron diffraction (SAED) patterns in Fig. 5g–i. Therefore, both Cu_6Sn_5 whiskers and protuberances exhibit the η'-Cu_6Sn_5 phase, while the matrix exhibits the η-Cu_6Sn_5 phase. Although no evidence of lattice compression is detected in the η-Cu_6Sn_5 matrix, these results can directly support our inference that the η'-Cu_6Sn_5 phase nucleates and grows on the surfaces of η-Cu_6Sn_5 bumps during ageing at 25 °C for 40 d In addition, the whisker elongates along the $[\bar{2}01]_{\eta'}$ direction with a side face of $(0\bar{2}0)_{\eta'}$; however, based on our XRD results, the surface texture of the whiskers should correspond to the $(204)_{\eta'}$ plane. The reason for this discrepancy may be cutting inaccuracy, as both $(0\bar{2}0)_{\eta'}$ and $(204)_{\eta'}$ share the same zone axis of $[\bar{2}01]_{\eta'}$. In other words, the actual side faces of the η'-Cu_6Sn_5 whiskers should be composed of $(204)_{\eta'}$ planes; this perfectly explains why the preferred orientation for Cu_6Sn_5 phase transformation in our XRD patterns changes from $(101)_\eta$+$(102)_\eta$ to $(204)_{\eta'}$.

Fig. 6a shows a TEM image of the bump matrix beneath the Cu_6Sn_5 whisker, and nearly parallel straight grain boundaries are observed across the entire matrix. All coloured lath-like grains marked have similar SAED patterns (as in Fig. 5i), indicating that they all split from one single-crystal matrix. Interestingly, a yellow grain, just beneath the whisker, protrudes outward from the matrix (white box in Fig. 6a); this extrusion feature implies that the grain splitting of η-Cu_6Sn_5 bumps is caused by the release of

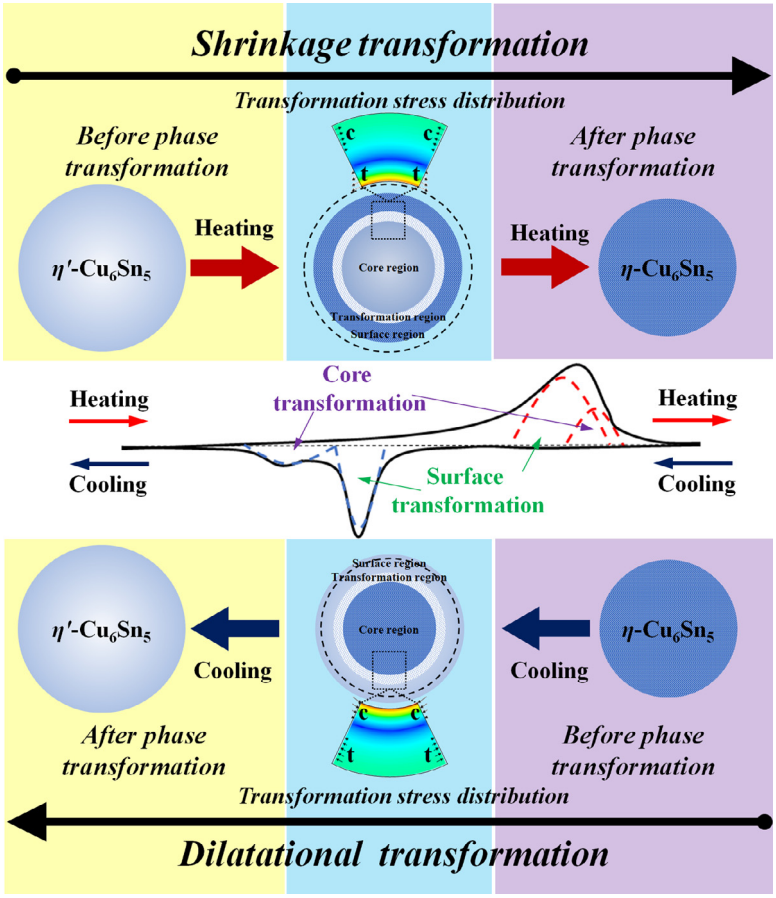

Fig. 4. Kinetic models of the structure-/stress-dependant phase transformation in Cu_6Sn_5. The transformation stress distributions in Cu_6Sn_5 particles are simulated based on the volumetric change during the phase transformation (compressive and tensile stresses are denoted "c" and "t", respectively). In addition, the latent heat peaks are marked based on the location of the phase transformation.

compressive stress inside the matrix. Moreover, according to the TEM-EDS analysis in Fig. 6b, the concentration of Cu in η-Cu_6Sn_5 is slightly higher than that in η'-Cu_6Sn_5, and an obvious increase in Cu content is detected at the interface. The finding of Cu segregation at the η-Cu_6Sn_5|η'-Cu_6Sn_5 interface can directly prove the existence of interfacial atomic segregation and clarify that the Cu_6Sn_5 phase transformation is diffusive in nature, rather than displacive.

4. Discussion

4.1. Atomistic simulation of whisker growth

Notably, the neighbouring η'-Cu_6Sn_5 grains in Fig. 5c present two different orientation relationships with the same η-Cu_6Sn_5 single-crystal matrix, but only one grain becomes a whisker. This result means that the nucleation may be random, but only certain growth can proceed unhindered. To further explore the reason for whisker growth, two atomic 3D configurations with interfaces between *matrix C* and *whisker A* and between *matrix C* and *protuberance B* are displayed in Fig. 7a and b, respectively. The initial orientation alignments are in accordance with our observations in Fig. 5d–f. The Cu and Sn atoms are coloured by red and blue, respectively. The oblique rectangle in the centre of the configuration denotes the position of the interface. Fig. 7c and d depict the corresponding evolution snapshots for in-plane atomic arrangements of $(1\bar{2}10)_\eta$|$(102)_{\eta'}$ and $(1\bar{2}10)_\eta$|$(3\bar{5}6)_{\eta'}$, respectively, during equilibrium at 400 K for 0–1.5 ps. The atomic behaviour is characterized by both shear strain and displacement from the reference configuration at time 0. The displacement vector is denoted by a yellow arrow, and the colourbar describes the degree of shear strain accumulation of an individual atom due to the relative motion of its neighbours. At 0 ps, the $(1\bar{2}10)_\eta$|$(102)_{\eta'}$ interface has a higher coherent degree than that of the $(1\bar{2}10)_\eta$|$(3\bar{5}6)_{\eta'}$ interface, and the distortion of atoms near the former interface is much smaller than that near the latter. At 0.5–1.5 ps, the atoms in η-Cu_6Sn_5 are subject to considerable stress, leading to a larger shear strain accumulation compared to those in η'-Cu_6Sn_5. The right-directed atomic movements in η-Cu_6Sn_5 indicate that this phase is unstable at this temperature and will thermodynamically transform to the η'-Cu_6Sn_5 phase. In addition, the closer to the interface, the larger the degree of shear strain accumulation is; meanwhile, the segregation of Cu atoms can also be observed, accompanying the shear strain accumulation at the interface shown in Fig. 7e and f (consistent with our experimental result shown in Fig. 6b). Hence, the segregations of both Cu atoms and shear strains can be detected at the interface (*see Movies S1 and S2 in the Supporting Information*).

Interestingly, the $(1\bar{2}10)_\eta$|$(102)_{\eta'}$ interface remains almost straight and moves parallel to the η-Cu_6Sn_5 phase (Fig. 7c). Although local segregations of atoms and shear strains occur close to this interface, the limited atomic displacements indicate that lattice reconstruction can be easily achieved by the short-range diffusion of atoms. In contrast, the evolution of the $(1\bar{2}10)_\eta$|$(3\bar{5}6)_{\eta'}$ interface results in a serrated structure (Fig. 7d). The segregation levels of atoms and shear strains at this interface are much higher than those at the $(1\bar{2}10)_\eta$|$(102)_{\eta'}$ interface; the atomic

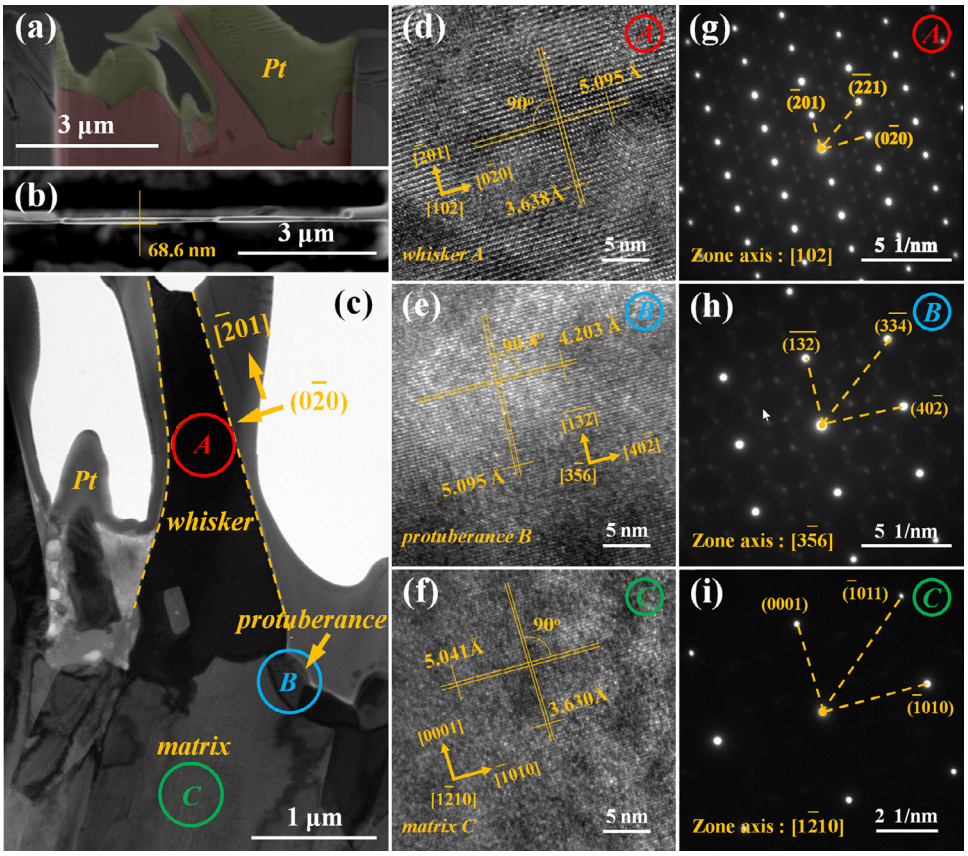

Fig. 5. Microstructures of a 40-d-aged Cu_6Sn_5 bump after FIB cutting: (a) SEM image in the cross-sectional direction; (b) SEM image in the top-view direction; and (c) TEM image. In addition, high-magnification TEM images and corresponding SAED patterns of the three regions of interest are shown in (d–f) and (g–i), respectively (For interpretation of the references to color in this figure, the reader is referred to the web version of this article.).

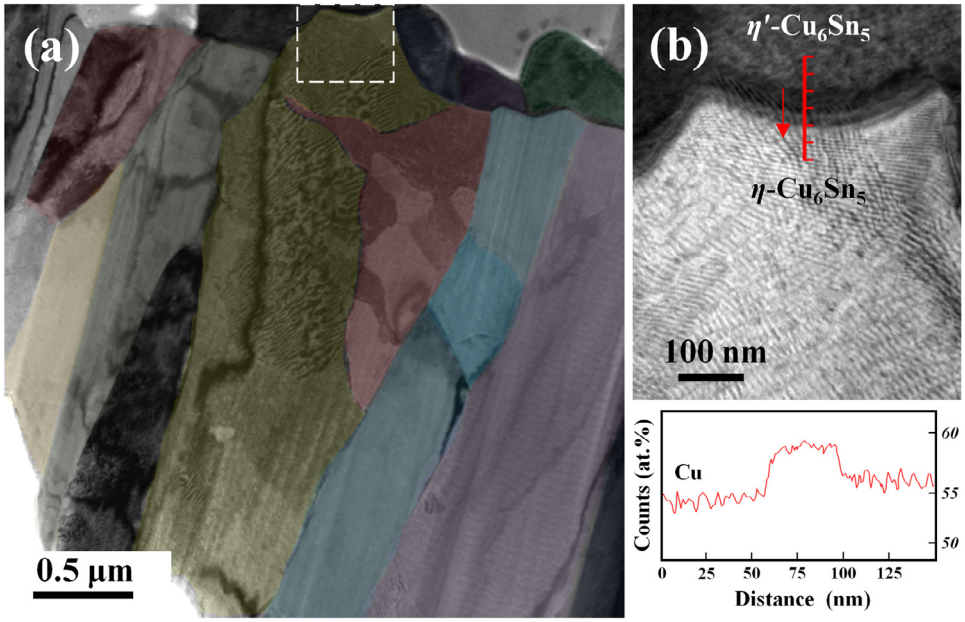

Fig. 6. (a) TEM image of the bump matrix beneath the Cu_6Sn_5 whisker in Fig. 5c. (b) Locally magnified TEM image of the *whisker-A*|*matrix-C* interface and the Cu distribution along the red line scanned using TEM-EDS.

displacements are also very chaotic, implying that the atoms need long-range diffusion to relax the structure and strain energy. More importantly, this interface shows no signs of tending towards stability. Although certain relatively stable regions are formed along the $[331]_{\eta'}$ direction, regions with large segregations of shear strains and atoms are found in both η-Cu_6Sn_5 and η'-Cu_6Sn_5. Overall, from the viewpoints of both thermodynamics and kinetics, the η'-Cu_6Sn_5 phase grows along the $(1\bar{2}10)_{\eta}\|(102)_{\eta'}$ interface much easier and faster than it grows along the $(1\bar{2}10)_{\eta}\|(3\bar{5}6)_{\eta'}$ interface; thus, the interfacial orientation relationship favourable for whisker growth can be expressed as follows: $(0001)_{\eta}\|(\bar{2}01)_{\eta'}$ and $[1\bar{2}10]_{\eta}\|[102]_{\eta'}$.

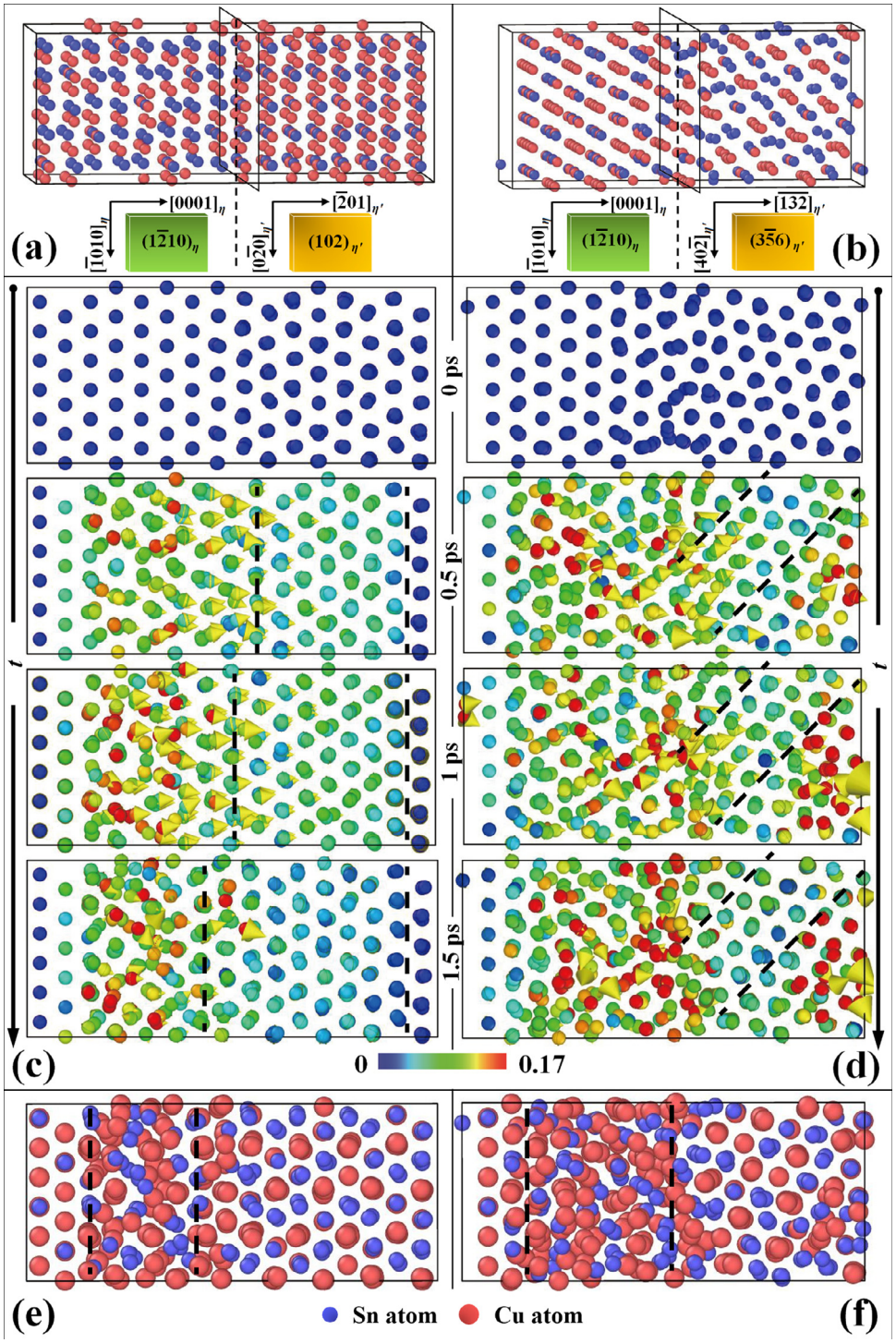

Fig. 7. Atomic 3D configurations with the (a) *matrix-C|whisker-A* and (b) *matrix-C|protuberance-B* interfaces and corresponding evolution snapshots for in-plane atomic arrangements of (c) $(1\bar{2}10)_{\eta}|(102)_{\eta'}$ and (d) $(1\bar{2}10)_{\eta}|(3\bar{5}6)_{\eta'}$ at 400 K for 0–1.5 ps. In addition, the corresponding atomic distributions of the two interfaces (*i.e.*, an evolution snapshot at 1.5 ps) are shown in (e) and (f), respectively (For interpretation of the references to color in this figure, the reader is referred to the web version of this article.).

4.2. Whisker growth mechanism and inhibition methods

The existence of local breaks in the surface oxide and the occurrence of compressive stress in the matrix are generally accepted as two necessary conditions for the formation of Sn whiskers [41]. Similarly, when the retarded transformation from η-Cu_6Sn_5 to η'-Cu_6Sn_5 occurs, a continuous monolayer of η'-Cu_6Sn_5 nuclei will be generated on the surfaces of the η-Cu_6Sn_5 bumps, and the resultant segregations of Cu atoms and shear strains at the η'-$Cu_6Sn_5|\eta$-Cu_6Sn_5 interface will undoubtedly block the release of compressive stress in the matrix (*see the Graphical Abstract*). However, if certain η'-Cu_6Sn_5 nuclei with favourable orientations are formed, then their low segregation levels may promote the occurrence of a phase transformation, triggering the formation of η'-Cu_6Sn_5 whiskers. Because sustained whisker growth will induce localized stress relief, a stress gradient may be created in the matrix, producing grain splitting of the η-Cu_6Sn_5 bumps. Moreover, the formation of η'-Cu_6Sn_5 protuberances will also crack the

bump surfaces, and long narrow gullies are observed in Fig. 1b. Hence, the phase-transformation-induced whisker growth, on the one hand, can bridge adjacent joints, causing electrical failure, and, on the other hand, may produce surface cracking and matrix splitting, making the joints more vulnerable to stress. Note that the sample in Fig. 6a wrinkled and shattered after observation, and this result directly documents the brittleness of Cu_6Sn_5 and the potential harmfulness of the retarded transformation from η-Cu_6Sn_5 to η'-Cu_6Sn_5.

To inhibit this retarded transformation, one method is to stabilize the η-Cu_6Sn_5 phase at low temperature; *e.g.*, minor additions of Ni, Zn, and Au have been reported to stabilize η-Cu_6Sn_5 at room temperature [42,43]. Moreover, methods of adjusting the cooling process may be effective in reducing the content of unreacted η-Cu_6Sn_5 in Cu_6Sn_5 IMC joints, *e.g.*, by slowing the cooling rate or providing proper thermal insulation during cooling [44,45]. In addition, for actual Cu_6Sn_5 flip-chip joints, whisker growth and matrix splitting may occur vertically in the sidewalls of the joints; therefore, underfill encapsulation may be the best method to protect Cu_6Sn_5 IMC joints in 3D ICs.

5. Conclusions

1. Surface reconstructions of quenched Cu_6Sn_5 bumps in terms of both microstructure and orientation were observed during ageing at 25 °C for 1–40 d Due to the retarded phase transformation from η-Cu_6Sn_5 to η'-Cu_6Sn_5, η'-Cu_6Sn_5 protuberances and whiskers were generated on the surfaces of η-Cu_6Sn_5 bumps via the nucleation-growth process. The compressive transformation stress was confirmed inside the bump matrix, and the phase-transformation-induced evolution of the surface texture was detected as $(101)_\eta+(102)_\eta\rightarrow(204)_{\eta'}$.
2. The kinetics of the Cu_6Sn_5 phase transformation are both structure dependent and stress dependent. When the dilatational transformation from η-Cu_6Sn_5 to η'-Cu_6Sn_5 occurs during cooling, the compressive stress generated in the particle cores cannot be easily released, producing a left shift of the corresponding exothermic peak. The smaller the particle size is, the less the stress accumulates in the cores and the more similar the shapes of the two heating-cooling curves.
3. Based on TEM observation, a η'-Cu_6Sn_5 whisker grows along the $[\bar{2}01]_{\eta'}$ direction with a side face of $(204)_{\eta'}$, and the orientation relationship between the two phases favourable for whisker growth is $(0001)_\eta\|(\bar{2}01)_{\eta'}$ and $[1\bar{2}10]_\eta\|[102]_{\eta'}$. The interfacial segregations of shear strains and Cu atoms are confirmed to play an important role in blocking the phase transformation from η-Cu_6Sn_5 to η'-Cu_6Sn_5 by AIMD simulation.
4. The existence of a segregation layer on the surface and the occurrence of compressive transformation stress in the matrix are two necessary conditions for the formation of η'-Cu_6Sn_5 whiskers. The whisker growth can bridge adjacent joints and produce surface cracking and matrix splitting. Three methods to inhibit whisker growth are proposed, and this study may help improve the reliability of entire Cu_6Sn_5 IMC joints in 3D ICs.

Declaration of Competing Interest

The authors declare that they have no known competing financial interests or personal relationships that could have appeared to influence the work reported in this paper.

Acknowledgments

This work was financially supported by the Fundamental Research Funds for the Central Universities under Grant No. 20720170053, Natural Science Foundation of Fujian Province of China under Grant No. 2018J01081, the Natural Science Foundation of Guangdong Province of China under Grant No. 2018A030313415, and the Fundamental Research Project of Shenzhen under Grant No. JCYJ20170306141647600.

Supplementary materials

Supplementary material associated with this article can be found, in the online version, at doi:10.1016/j.actamat.2019.11.032.

References

[1] H.Y. Hsiao, C.M. Liu, H.W. Lin, T.C. Liu, C.L. Lu, Y.S. Huang, C. Chen, K.N. Tu, Unidirectional growth of microbumps on (111)-Oriented and nanotwinned copper, Science 336 (2012) 1007–1010.
[2] G. Zeng, S.D. McDonald, J.J. Read, Q. Gu, K. Nogita, Kinetics of the polymorphic phase transformation of Cu_6Sn_5, Acta Mater 69 (2014) 135–148.
[3] M.L. Huang, J.F. Zhao, Z.J. Zhang, N. Zhao, Dominant effect of high anisotropy in β-Sn grain on electromigration-induced failure mechanism in Sn-3.0ag-0.5cu interconnect, J. Alloy. Compd. 678 (2016) 370–374.
[4] Z.L. Ma, S.A. Belyakov, K. Sweatman, T. Nishimura, T. Nishimura, C.M. Gourlay, Harnessing heterogeneous nucleation to control tin orientations in electronic interconnections, Nat. Commun. 8 (2017) 1916.
[5] Z.H. Zhang, M.Y. Li, Z.Q. Liu, S.H. Yang, Growth characteristics and formation mechanisms of Cu_6Sn_5 phase at the liquid-Sn0.7Cu/(111)(Cu) and liquid-Sn0.7Cu/(001)(Cu) joint interfaces, Acta Mater. 104 (2016) 1–8.
[6] J.W. Xian, Z.L. Ma, S.A. Belyakov, M. Ollivier, C.M. Gourlay, Nucleation of tin on the Cu_6Sn_5 layer in electronic interconnections, Acta Mater 123 (2017) 404–415.
[7] J.W. Xian, S.A. Belyakov, M. Ollivier, K. Nogita, H. Yasuda, C.M. Gourlay, Cu_6Sn_5 crystal growth mechanisms during solidification of electronic interconnections, Acta Mater 126 (2017) 540–551.
[8] M.S. Park, R. Arróyave, Early stages of intermetallic compound formation and growth during lead-free soldering, Acta Mater 58 (2010) 4900–4910.
[9] J.H. Ke, Y. Gao, C.R. Kao, Y. Wang, Pattern formation during interfacial reaction in-between liquid sn and cu substrates - A simulation study, Acta Mater 113 (2016) 245–258.
[10] Y.X. Liu, Y.C. Chu, K.N. Tu, Scaling effect of interfacial reaction on intermetallic compound formation in Sn/Cu pillar down to 1μm diameter, Acta Mater 117 (2016) 146–152.
[11] Z.H. Zhang, H.J. Cao, M.Y. Li, Y.X. Yu, H.F. Yang, S.H. Yang, Three-dimensional placement rules of Cu_6Sn_5 textures formed on the $(111)_{Cu}$ and $(001)_{Cu}$ surfaces using electron backscattered diffraction, Mater. Design. 94 (2016) 280–285.
[12] J.W. Xian, G. Zeng, S.A. Belyakov, Q. Gu, K. Nogita, C.M. Gourlay, Anisotropic thermal expansion of Ni_3Sn_4, Ag_3Sn, Cu_3Sn, Cu_6Sn_5 and β-Sn, Intermetallics 91 (2017) 50–64.
[13] Y.Q. Wu, J.C. Barry, T. Yamamoto, Q.F. Gu, S.D. McDonald, S. Matsumura, H. Huang, K. Nogita, A new phase in stoichiometric Cu_6Sn_5, Acta Mater 60 (2012) 6581–6591.
[14] T.L. Yang, T. Aoki, K. Matsumoto, K. Toriyama, A. Horibe, H. Mori, Y. Orii, J.Y. Wu, C.R. Kao, Full intermetallic joints for chip stacking by using thermal gradient bonding, Acta Mater 113 (2016) 90–97.
[15] V.L. Nguyen, C.S. Chung, H.K. Kim, Comparison of the fracture toughness of Cu_6Sn_5 intermetallic compound as measured by nanoindentation and other methods, Mater. Lett. 162 (2016) 185–190.
[16] B. Philippi, K. Matoy, J. Zechner, C. Kirchlechner, G. Dehm, Fracture toughness of intermetallic Cu_6Sn_5 in lead-free solder microelectronics, Scr. Mater. 123 (2016) 38–41.
[17] W.Y. Li, X.P. Zhang, H.B. Qin, Y.W. Mai, Joule heating dominated fracture behavior change in micro-scale cu/sn-3.0ag-0.5cu/cu(ni) joints under electro-thermal coupled loads, Microelectron. Reliab. 82 (2018) 224–227.
[18] Y. Goh, A.S.M.A. Haseeb, H.L. Liew, M.F.M. Sabri, Deformation and fracture behaviour of electroplated Sn–Bi/Cu solder joints, J. Mater. Sci. 50 (2015) 4258–4269.
[19] H.T. Lee, K.C. Huang, Effect of solder joint geometry on the low-cycle fatigue behavior of Sn-xag-0.7CU, J. Electron. Mater. 45 (2016) 6102–6112.
[20] J. Gu, Y. Lei, J. Lin, H. Fu, Z. Wu, The failure models of lead free sn-3.0ag-0.5cu solder joint reliability under low-g and high-g drop impact, J. Electron. Mater. 46 (2016) 1396–1404.
[21] Y.B. Kar, T.C. Hui, R. Agileswari, C. Lo, Comparison study on reliability performance for polymer core solder balls under multiple reflow and HTS stress tests, Microelectron. Reliab. 53 (2013) 164–173.
[22] J. Wang, H. Nishikawa, Impact strength of Sn–3.0AG–0.5Cu solder bumps during isothermal aging, Microelectron. Reliab. 54 (2014) 1583–1591.
[23] J. Gu, J. Lin, Y. Lei, H. Fu, Experimental analysis of Sn-3.0Ag-0.5Cu solder joint board-level drop/vibration impact failure models after thermal/isothermal cycling, Microelectron. Reliab. 80 (2018) 29–36.
[24] J.H. Ke, H.Y. Chuang, W.L. Shih, C.R. Kao, Mechanism for serrated cathode dissolution in Cu/Sn/Cu interconnect under electron current stressing, Acta Mater 60 (2012) 2082–2090.
[25] Y.C. Chan, D. Yang, Failure mechanisms of solder interconnects under current stressing in advanced electronic packages, Prog. Mater. Sci. 55 (2010) 428–475.

[26] C.F. Lin, S.H. Lee, C.M. Chen, Effect of sn grain orientation on the Cu_6Sn_5 formation in a Sn-based solder under current stressing, Metall. Mater. Trans. A 43 (2012) 2571–2573.
[27] Z.H. Zhang, H.J. Cao, M.Y. Li, Y. Wang, Z.Q. Liu, Cathodic peeling damage of Cu_6Sn_5 phase in Cu/$SnAg_{3.0}Cu_{0.5}$/Cu bridge interconnections under current stressing, J. Appl. Phys. 116 (2014) 054909.
[28] H. Chen, M. Mueller, T.T. Mattila, J. Li, X. Liu, K.J. Wolter, M. Paulasto-Kröckel, Localized recrystallization and cracking of lead-free solder interconnections under thermal cycling, J. Mater. Res. 26 (2011) 2103–2116.
[29] Y.G. Sung, W.R. Myung, H. Jeong, M.K. Ko, J. Moon, S.B. Jung, Mechanical reliability of the epoxy Sn-58wt.%Bi solder joints with different surface finishes under thermal shock, J. Electron. Mater. 47 (2018) 4165–4169.
[30] H.M. Lin, C.Y. Ho, W.L. Chen, Y.H. Wu, D.H. Wang, J.R. Lin, Y.H. Wu, H.C. Hong, Z.W. Lin, J.G. Duh, Interfacial reaction and mechanical evaluation in multi--level assembly joints with enepig under bump metallization via drop and high speed impact test, Microelectron. Reliab. 55 (2015) 231–237.
[31] C.C. Tuan, N.P. James, Z. Lin, Y. Chen, Y. Liu, K.S. Moon, Z. Li, C.P. Wong, Self--patterning of silica/epoxy nanocomposite underfill by tailored hydrophilic–superhydrophobic surfaces for 3D integrated circuit (IC) stacking, ACS Appl. Mater. Inter. 9 (2017) 8437–8442.
[32] K. Nogita, D. Mu, S.D. McDonald, J. Read, Y.Q. Wu, Effect of Ni on phase stability and thermal expansion of $Cu_{6-x}Ni_xSn_5$ (X = 0, 0.5, 1, 1.5 and 2), Intermetallics 26 (2012) 78–85.
[33] U. Schwingenschlögl, C. Di Paola, K. Nogita, C.M. Gourlay, The influence of Ni additions on the relative stability of η; and η'; Cu_6Sn_5, Appl. Phys. Lett. 96 (2010) 061908.
[34] K. Nogita, C.M. Gourlay, S.D. McDonald, Y.Q. Wu, J. Read, Q.F. Gu, Kinetics of the η;–η'; transformation in Cu_6Sn_5, Scr. Mater. 65 (2011) 922–925.
[35] M.Y. Li, Z.H. Zhang, J.M. Kim, Polymorphic transformation mechanism of η; and η'; in single crystalline Cu_6Sn_5, Appl. Phys. Lett. 98 (2011) 201901.
[36] G. Ghosh, M. Asta, Phase Stability, Phase transformations, and elastic properties of Cu_6Sn_5: ab initio calculations and experimental results, J. Mater. Res. 20 (2005) 3102–3117.
[37] J.P. Perdew, K. Burke, M. Ernzerhof, Generalized gradient approximation made simple, Phys. Rev. Lett. 77 (1996) 3865–3868.
[38] P.E. Blöchl, Projector augmented-wave method, Phys. Rev. B 50 (1994) 17953–17979.
[39] J.O. Suh, K.N. Tu, N. Tamura, Dramatic morphological change of scallop-type Cu_6Sn_5 formed on (001) single crystal copper in reaction between molten Snpb solder and cu, Appl. Phys. Lett. 91 (2007) 051907.
[40] M.V. Castro, C.J. Tavares, Dependence of Ga-doped Zno thin film properties on different sputtering process parameters: substrate temperature, sputtering pressure and bias voltage, Thin Solid Films 586 (2015) 13–21.
[41] T.C. Chiu, K.L. Lin, The growth of sn whiskers with dislocation inclusion upon electromigration through a Cu/Sn3.5Ag/Au solder joint, Scripta Mater. 60 (2009) 1121–1124.
[42] G. Zeng, S.D. McDonald, Q. Gu, K. Nogita, Effect of Zn, Au, and In on the polymorphic phase transformation in Cu_6Sn_5 intermetallics, J. Mater. Res. 27 (2012) 2609–2614.
[43] Y.Q. Wu, S.D. McDonald, J. Read, H. Huang, K. Nogita, Determination of the minimum Ni concentration to prevent the η; to η;$^{4+1}$ polymorphic transformation of stoichiometric Cu_6Sn_5, Scripta Mater 68 (2013) 595–598.
[44] Z.H. Zhang, C.W. Weri, H.J. Cao, J.J. Han, Y. Zhang, Structure-induced metastable phase transformation in Cu_6Sn_5 intermetallics, Mater. Lett. 249 (2019) 124–127.
[45] F. Somidin, S.D. McDonald, X.Z. Ye, D.D. Qu, K. Sweatman, T. Akaiwa, T. Nishimura, K. Nogita, Inhibition of cracking in Cu_6Sn_5 intermetallic compounds at the interface of lead-free solder joint by controlling the reflow cooling conditions, In:ICEP (2019) 223–228 http://dx.doi.org/10.23919/ICEP.2019.8733594.